SOFIA's Secondary Mirror Assembly: In-Flight Performance and Control Approach

Andreas Reinacher[a,b], Yannick Lammen[a,b], and Hans-Peter Roeser[c]

[a]Deutsches SOFIA Institut, University of Stuttgart, Pfaffenwaldring 29, 70569 Stuttgart, Germany
[b]SOFIA Airborne Systems Operations Center, NASA Armstrong Flight Research Center, Mail Stop AFRC Bldg. 703, S241, P.O. Box 273, Edwards CA 93523, USA
[c]Institute of Space Systems, University of Stuttgart, Pfaffenwaldring 29, 70569 Stuttgart, Germany

ABSTRACT

The Stratospheric Observatory for Infrared Astronomy (SOFIA) is a 2.5 m infrared telescope built into a Boeing 747 SP. In 2014 SOFIA reached its Full Operational Capability milestone and nowadays takes off about three times a week to observe the infrared sky from altitudes above most of the atmosphere's water vapor content. An actively controlled 352 mm SiC secondary mirror is used for infrared chopping with peak-to-peak amplitudes of up to 10 arcmin and chop frequencies of up to 20 Hz and also as actuator for fast pointing corrections. The Swiss-made Secondary Mirror Mechanism (SMM) is a complex, highly integrated and compact flexure based mechanism that has been performing with remarkable reliability during recent years. Above mentioned capabilities are provided by the Tilt Chopper Mechanism (TCM) which is one of the two stages of the SMM. In addition the SMM is also used to establish a collimated telescope and to adjust the telescope focus depending on the structure's temperature which ranges from about 40° C at takeoff in Palmdale, CA to about −40° C in the stratosphere. This is achieved with the Focus Center Mechanism (FCM) which is the base stage of the SMM on which the TCM is situated.

Initially the TCM was affected by strong vibrations at about 300 Hz which led to unacceptable image smearing. After some adjustments to the PID-type controller it was finally decided to develop a completely new control algorithm in state space. This pole placement controller matches the closed loop system poles to those of a Bessel filter with a corner frequency of 120 Hz for optimal square wave behavior. To reduce noise present on the position and current sensors and to estimate the velocity a static gain Kalman Filter was designed and implemented. A system inherent delay is incorporated in the Kalman filter design and measures were applied to counteract the actuators' hysteresis. For better performance over the full operational temperature range and to represent an amplitude dependent non-linearity the underlying model of the Kalman filter adapts in real-time to those two parameters. This highly specialized controller was developed over the course of years and only the final design is introduced here.

The main intention of this contribution is to present the currently achieved performance of the SOFIA chopper over the full amplitude, frequency, and temperature range. Therefore a range of data gathered during in-flight tests aboard SOFIA is displayed and explained. The SMM's three main performance parameters are the transition time between two chop positions, the stability of the Secondary Mirror when exposed to the low pressures, low temperatures, aerodynamic, and aeroacoustic excitations present when the SOFIA observatory operates in the stratosphere at speeds of up to 850 km/h, and finally the closed-loop bandwidth available for fast pointing corrections.

Keywords: SOFIA, chopper, secondary mirror, control, performance

---

Further author information: A.R.: reinacher@dsi.uni-stuttgart.de, www.dsi.uni-stuttgart.de, www.nasa.gov/sofia

Ground-based and Airborne Instrumentation for Astronomy VI, edited by Christopher J. Evans, Luc Simard, Hideki Takami
Proc. of SPIE Vol. 9908, 99082V · © 2016 SPIE · CCC code: 0277-786X/16/$18 · doi: 10.1117/12.2232851

1. INTRODUCTION

SOFIA, the Stratospheric Observatory for Infrared Astronomy, reached its Full Operational Capability (FOC) in February 2014, completed a major aircraft maintenance check the same year, commissioned all of its first generation science instruments, and already started commissioning a second generation instrument. Currently, SOFIA conducts its third southern hemisphere deployment in Christchurch, New Zealand. So SOFIA is in full swing, filling the gap in infrared and submillimeter astronomy left behind when Herschel had to suspend operations.

In SOFIA's targeted wavelength band of $0.3\,\mu\text{m} - 1.6\,\text{mm}$ chopping is an indispensable technique for many observations. Alternating up to twenty times per second between the science object and the infrared background to multiply the signal to noise ration is done with the SOFIA Secondary Mirror Assembly (SMA) which is depicted in figure 1 along with its location on the SOFIA telescope. The three sub-assemblies of the SMA are the Focus Center Mechanism (FCM), which is located in the SMA's base which is attached to the telescope's spider arms. It is a hexapod type mechanism with five degrees of freedom (DOF, rotation around the line of sight axis is blocked) to adjust the telescope focus and its collimation.

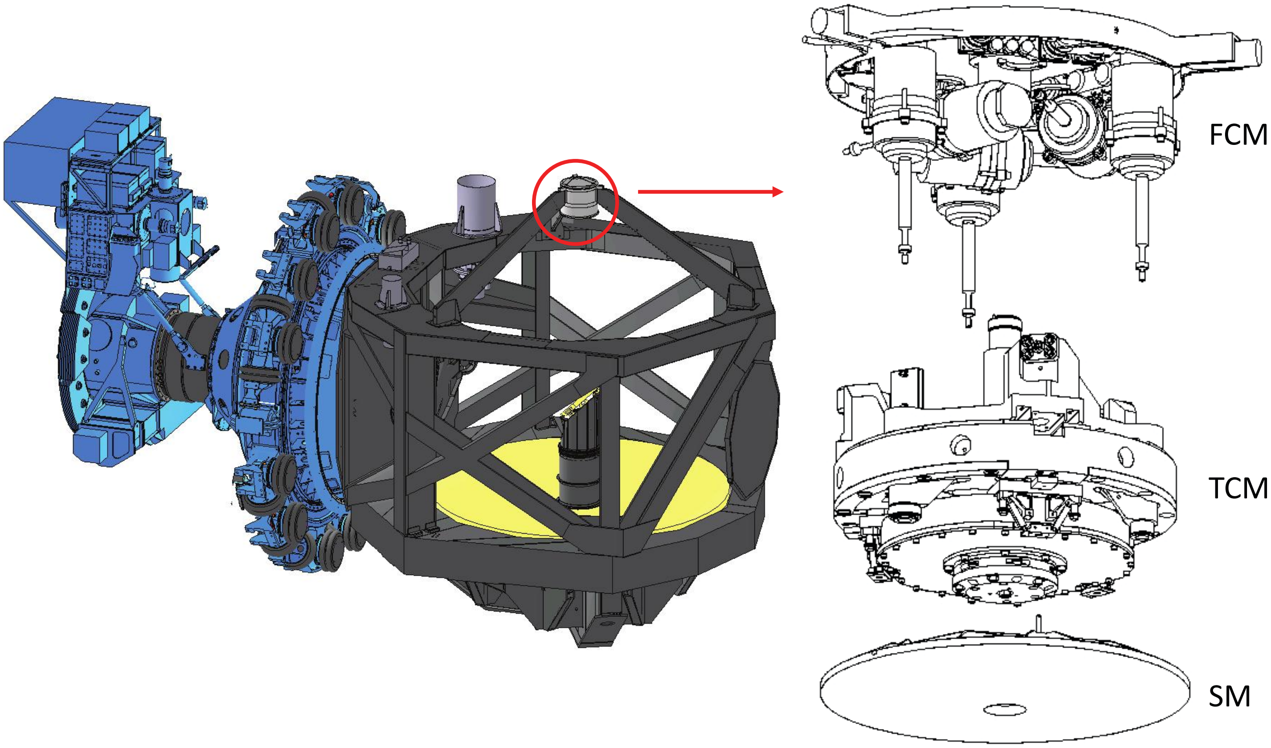

Figure 1: The SMM in the SOFIA Telescope

Attached to the FCM is the Tilt Chop Mechanism (TCM) which has two DOF, the rotations in tip and tilt which can be combined as required to adjust the rotation axis. It is capable of chopping with up to 20 Hz with amplitudes of up to 1125 arcsec which translates into a chop throw of 10 arcmin on the sky. It is also used for pointing corrections which exceed the bandwidth of the telescope's main drive assembly.

The TCM drives the stiff and lightweight Secondary Mirror (SM) made of Silicon Carbide (SiC) and measuring 352 mm in diameter. The connection consists of flexure type bipods to compensate for the different coefficients of thermal expansion of Aluminum (TCM) and SiC.

Due to the exposed position of the SMA in the telescope cavity it is subject to significant aerodynamic and aeroacoustic excitations when the cavity door which covers the aircraft fuselage during takeoff and landing opens up in the stratosphere. This makes great demands on the TCM controller's disturbance rejection capabilities. Challenging is also the required precision of SMM moves while operating in a wide temperature range of around 80 °C. The major performance parameter, however, is the transition time between two chop positions. This become clear when considering an exemplary observation of one hour with a typical chop frequency of 5 Hz. That sums up to 36, 000 chop transitions for this observation alone.

The controller design resulting of these, in parts contradictory, requirements is explained in chapter 3 with the preceding chapter 2 showing the design of the state space model used for the development of the controller and as real-time state estimator in form of a Kalman filter. Chapter 4 presents recent results of performance tests conducted in flight with this controller.

2. SYSTEM IDENTIFICATION AND MODEL DESIGN

The TCM is actuated with three linear motors with moving magnets, arranged in an axially symmetric 120° pattern as shown in figure 2. The motors sit close to the center and actuate respective levers which transmit the motion to the Intermediate Plate which holds the mirror and at the same time to the ring-shaped Compensation Mass (Intermediate Plate, mirror and Compensation Mass not shown in figure 2). Figure 3 shows a schematic and a sectional view of the system. The lever arms, the Compensation Mass, and the Intermediate Plate are tuned in such a way that when rotating the resulting forces on the supporting structure are minimized. All joints are made with flexure parts to minimize play and to have high stiffness to reduce susceptibility to wind loads. The distance of the Intermediate Plate relative to the TCM base, the Mobile Stage, is measured by three eddy current sensors collocated with the actuators.

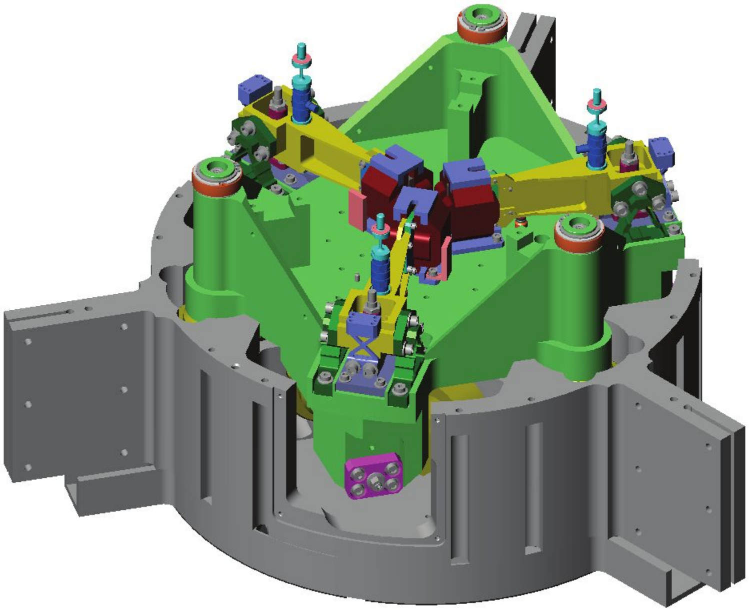

Figure 2: TCM actuator arrangement

For more information on the mechanical aspects of the SMM please refer to [1] and [2]. Information about recent maintenance and inspection activities performed on the SMM can be found in [3].

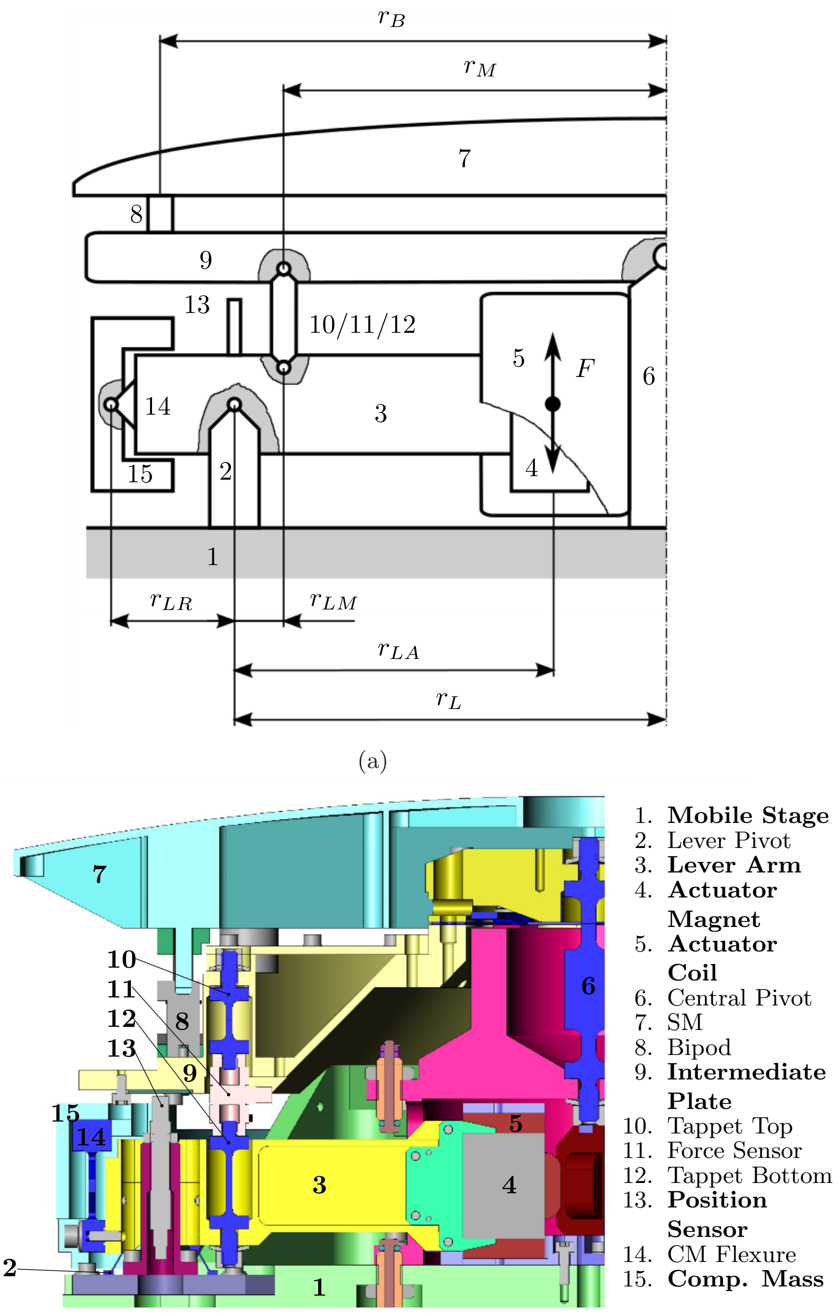

(a)

(b)

Figure 3: TCM schematics and sectional view

An initial model in the state space representation

$$\dot{\mathbf{x}} = \mathbf{A}\mathbf{x} + \mathbf{B}u, \tag{1}$$

of the TCM was derived in [4]. The state vector is defined as

$$\mathbf{x} = \begin{pmatrix} I_{R,S} \\ \dot{\xi}_{R,S} \\ \xi_{R,S} \end{pmatrix}, \tag{2}$$

with the actuator current $I_{R,S}$, the angular velocity $\dot{\xi}_{R,S}$, and the angular position $\xi_{R,S}$. R and S denote the tip and tilt direction. The state space matrix then becomes

$$\mathbf{A} = \begin{pmatrix} -\frac{R}{L} & -\frac{K_u \cdot r_{LA} \cdot r_M}{r_{LM} \cdot L} & 0 \\ \frac{K_F \cdot r_{LA} \cdot r_M}{r_{LM} \cdot \Theta_{R,S}} & -\frac{D_{R,S}}{\Theta_{R,S}} & -\frac{K_{R,S}}{\Theta_{R,S}} \\ 0 & 1 & 0 \end{pmatrix}. \tag{3}$$

The geometric distances are depicted in figure 3a, R and L are the actuators' electrical resistance and inductance, K_u and K_F are the back EMF and force constant of the actuators, $\Theta_{R,S}$ is the sum of the moments of inertia of all moving components, and $K_{R,S}$ and $D_{R,S}$ summarizes the stiffness and damping of the different joints.

The input command $u_{R,S}$ gets amplified by the amplifier gain K_A, so

$$U_{R,S} = K_A \cdot u_{R,S}, \tag{4}$$

and the input matrix becomes

$$\mathbf{B} = \begin{pmatrix} \frac{K_A}{L} \\ 0 \\ 0 \end{pmatrix}. \tag{5}$$

The states measured are $I_{R,S}$ and $\xi_{R,S}$, therefore the output matrix in

$$\mathbf{y} = \mathbf{C}\mathbf{x} \tag{6}$$

is

$$\mathbf{C} = \begin{pmatrix} 1 & 0 & 0 \\ 0 & 0 & 1 \end{pmatrix}. \tag{7}$$

The initial parameters in above equations were taken from data sheets and the CAD model and were then optimized to better fit system identification data recorded with the SMM in the SOFIA aircraft. Figure 4a shows the resulting excellent agreement between measurement and model in a frequency response plot from the input command voltage to the position output.

There are two eigenfrequencies at the upper end of the plotted frequency range, at $f_1 = 252\,\text{Hz}$ and $f_2 = 292\,\text{Hz}$ (later referred to as the 300 Hz mode). These can be modeled by adding pole zero pairs[5] to the transfer function. Please see table 1 for details.

A system inherent delay in the feedback path was modeled as a discrete two sample steps delay, i.e. a 5 ms delay in the 4 kHz sampled system. This was necessary to get the same good agreement in the phase plot as in the magnitude plot. A time plot of the two states angular position and actuator current for sine sweep and square wave excitation is shown in figure 4b. The similarity between measurement and model output confirms the high quality of the model.

This high quality, however, was only given in a certain amplitude and temperature range. The influence of both of these parameters has to be considered to have an adequate model output over the full temperature and

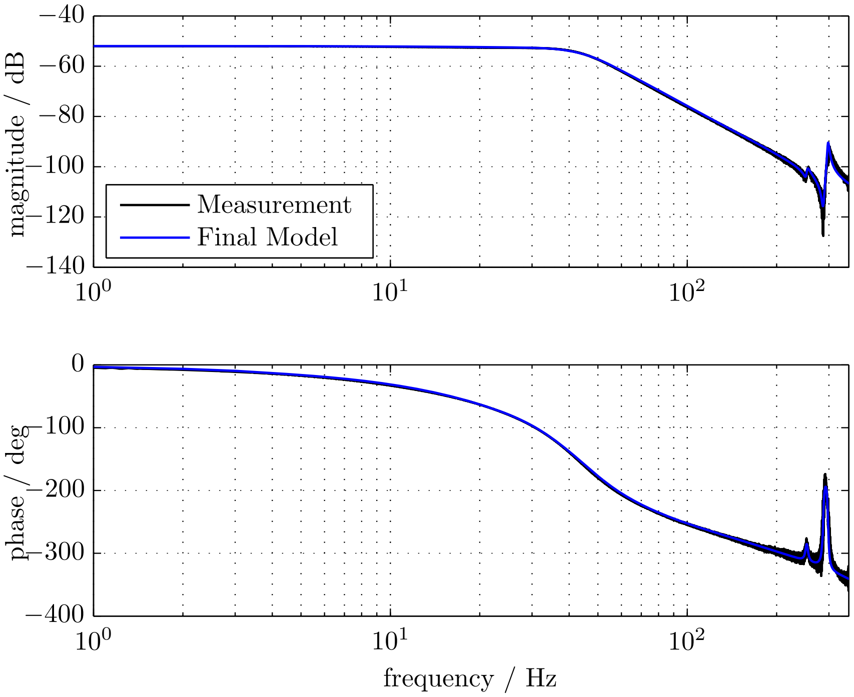

(a) Bode plot: Voltage to position

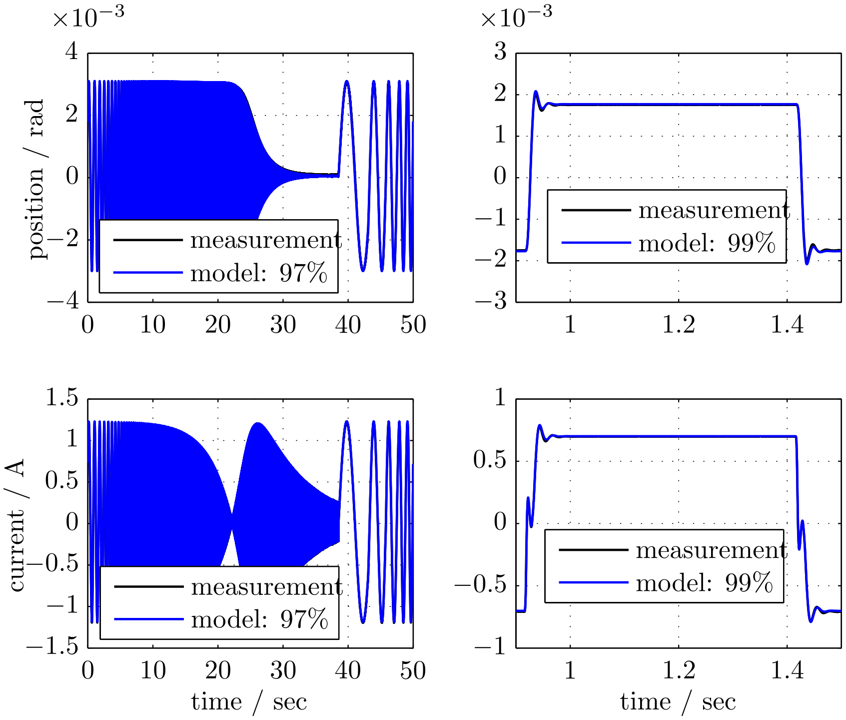

(b) Time plot of position and current

Figure 4: Model output vs. measurement

	frequency in Hz	damping
zero 1	251.8	0.012
pole 1	253.3	0.012
zero 2	287	0.009
pole 2	298	0.008

Table 1: Poles and zeros to model the eigenfrequencies

amplitude range. The temperature dependency can be modeled by replacing the actuator resistance R in the state matrix (3) with its temperature dependent equivalent

$$R_{\Delta T} = R_{20}(1 + \alpha_{20}\Delta T). \tag{8}$$

R_{20} is the electrical resistance at a temperature of $T = 20^\circ$ C, α_{20} is the temperature coefficient of resistance of copper, and $\Delta T = T - 20^\circ C$.

Analyzing data taken at various different amplitudes indicates nonlinear behavior of the TCM with changing deflections. By systematic variation of one parameter at a time and fitting the resulting Bode plots of the model to the measured data at different amplitudes over a wide frequency range, tweaking of the mechanism's stiffness was identified as the single most effective way to fit the model to reality. The actuators' force constant and back EMF constant also seem to contribute to the amplitude dependent behavior but to a much lesser, negligible degree than the stiffness.

Figure 5 shows the stiffness versus amplitude plot resulting from this approach. With a polynomial of 6^{th} order

$$\begin{aligned} K_{R,S} =& 4.433 \cdot 10^{-15} A_C^6 - 1.816 \cdot 10^{-11} A_C^5 + 2.983 \cdot 10^{-8} A_C^4 \\ & - 2.529 \cdot 10^{-5} A_C^3 + 0.01192 A_C^2 - 3.189 A_C + 2804 \end{aligned} \tag{9}$$

with the commanded deflection (chop amplitude or static tip/tilt) A_C in arc seconds a good curve fit was achieved as shown in figure 5 along with the residuals.

3. CONTROL APPROACH

As described in [6], a state space controller designed with pole placement was chosen to replace the previously implemented PID-type controller which strongly excited a flexible mode of the system at a frequency of 300 Hz. By matching the closed loop system poles to those of a Bessel filter optimal square wave behavior needed for chopping is achieved. Still, the mentioned structural eigenmode, a delay in the sensor feedback path of 0.65 ms, and noise on the position and current sensors limits the controller bandwidth.

All of these restraints could be attenuated by introducing an observer/Kalman filter[7] in the real-time control loop. The system model introduced in chapter 2 was discretized and coded into the control software. All states, the angular position, the angular velocity, and the actuator currents are now estimated with a steady-state Kalman filter based on the derived model. In addition, using the observer allows for the system to be controlled as if there was no output delay.[2]

Not only is the noise of the position and current measurements reduced by choosing the Kalman gain accordingly, but the angular velocity is calculated by the Kalman filter, rather than being differentiated from the measured position which led to very high noise on the velocity signal. However, great care must be taken when choosing the Kalman gain as to maintain reasonable disturbance rejection capabilities. Choosing the observer gains is basically a trade-off between using the estimated model output and using the sensor measurements as feedback into the controller. Relying too much on the model output results in a diminished disturbance rejection and a susceptibility to model errors.

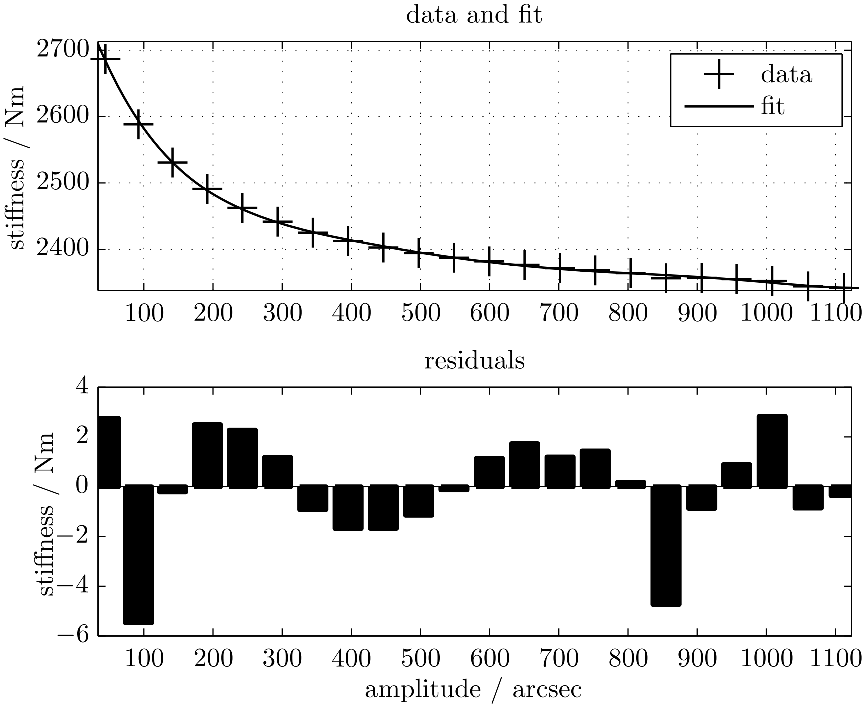

Figure 5: Stiffness vs. amplitude

To determine the Kalman gain, the covariance R of the measurement noise is required. For the position sensor noise v, R can be determined to be

$$E\{vv^T\} = R = I\sigma^2 = 1.2 \cdot 10^{-12} m^2, \tag{10}$$

which is the standard deviation of the position sensor measurement. Therefore the remaining design parameter to determine the Kalman gain is the covariance Q of the unknown process noise w:

$$E\{ww^T\} = Q. \tag{11}$$

An initial value for Q was determined by increasing it as far as possible without raising the RMS of the estimated position above the RMS of the position measurement in open loop with an idle TCM.

The closed loop performance depends, of course, also on the controller, i.e. for every set of controller poles the Q value needs to be determined anew for optimal results. This is done by decreasing the initially determined value of $Q = 5 \cdot 10^{-7}$, and therefore the measurement noise sensitivity until the closed loop performance without disturbance does not exhibit a higher position RMS value than the position sensors itself in open loop. In that way, it is assured that the best possible disturbance rejection is achieved without increasing the measurement noise.

As mentioned previously the controller gains were chosen to match the closed loop poles to those of a Bessel filter. Figure 6 shows the step response of fourth order (matches the model order) Bessel filters with corner frequencies between 100 and 200 Hz. All responses are very smooth with only minimal overshoot. By choosing the corner frequency of the Bessel filter the minimal settling time of the chopper will be defined.

Naturally, the faster the controller, the more the sensor noise gets amplified. Table 2 shows the maximally achievable $\mathbf{Q}$ values for Bessel filter controller poles with different corner frequencies.

If for a given observer the corner frequency of the Bessel filter is increased beyond the value in the table, the closed loop RMS position increases considerably. This is illustrated in figure 7, where a Kalman filter with $\mathbf{Q} = 1 \cdot 10^{-7}$ is combined with two different controllers. The controller poles are chosen so that the closed loop

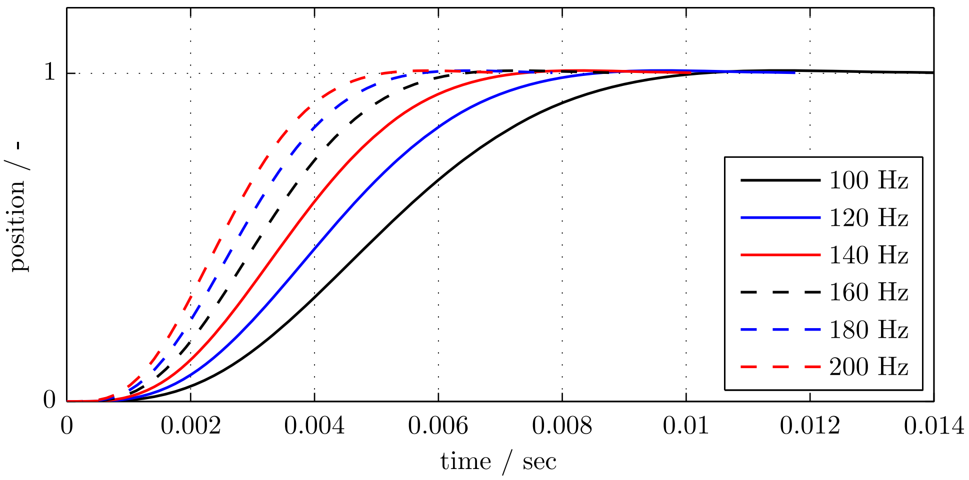

Figure 6: Step response of Bessel filters with different corner frequencies

Controller	90 Hz	110 Hz	120 Hz	130 Hz	140 Hz	150 Hz	190 Hz
Q value	$1 \cdot 10^{-7}$	$5 \cdot 10^{-8}$	$3 \cdot 10^{-8}$	$2 \cdot 10^{-8}$	$1 \cdot 10^{-8}$	$6 \cdot 10^{-9}$	$1 \cdot 10^{-9}$

Table 2: **Q** values for different controller poles

poles match a 90 and a 100 Hz Bessel filter, respectively.

The increase of the RMS position is concentrated at one frequency, the previously mentioned 300 Hz, which corresponds to a flexible mode. So increasing the controller gains leads to an excitation of this flexible mode. This is shown here for just one controller/observer combination, but it is true for all other combinations as well. For each set of Kalman filter gains the controller poles can be increased to a certain set of controller poles at which the RMS position value still remains below 0.3 arcsec. If either the Kalman gains or the controller gains are increased from there on the eigenfrequency at 300 Hz will be excited and the RMS value will increase abruptly.

So in general, there is a large number of controller/observer combinations to choose from. Which one to pick depends mainly on two performance parameters, one is the achieved settling time and the other is the disturbance rejection behavior. While minimizing the settling time requires maximizing the controller gains, it is somewhat more complex for the disturbance rejection. Generally the disturbance rejection improves with a faster controller, too, but as just shown, in the TCM case a faster controller requires a slower observer. But if the disturbance is not observed because the observer is too slow it can not be rejected.

So in terms of disturbance rejection the best gain sets can be determined on ground by injecting white noise as a simulated disturbance into the amplifiers and then determine the resulting movement. The illustration best suited for this analysis is the cumulative RMS plot because here the movement over the full frequency range is summed up.

Figure 8a shows such a plot for a range of different controller/observer gain sets. Only the controller gains are indicated, for the matching observer gains please refer to table 2. For reference the dashed line indicates how the disturbance impacts the position if the observer gains are set to zero, i.e. if there is no disturbance rejection. Figure 8b is zoomed into the low frequency end of the measured position cumulative RMS plot. Clearly, the controller which matches the closed-loop poles to a 120 Hz Bessel filter and the corresponding Kalman filter with $Q = 3 \cdot 10^{-8}$ offer the smallest position deviation added up over frequency. In other words, this combination offers the best disturbance rejection and was therefore chosen for permanent implementation.

How this controller/observer combinations ranks in term of settling time is shown in figure 9. As expected, the slope of the transient gets steeper with rising Bessel filter cutoff frequency. The resulting settling times for a chop amplitude of 100 arcsec are listed in table 3.

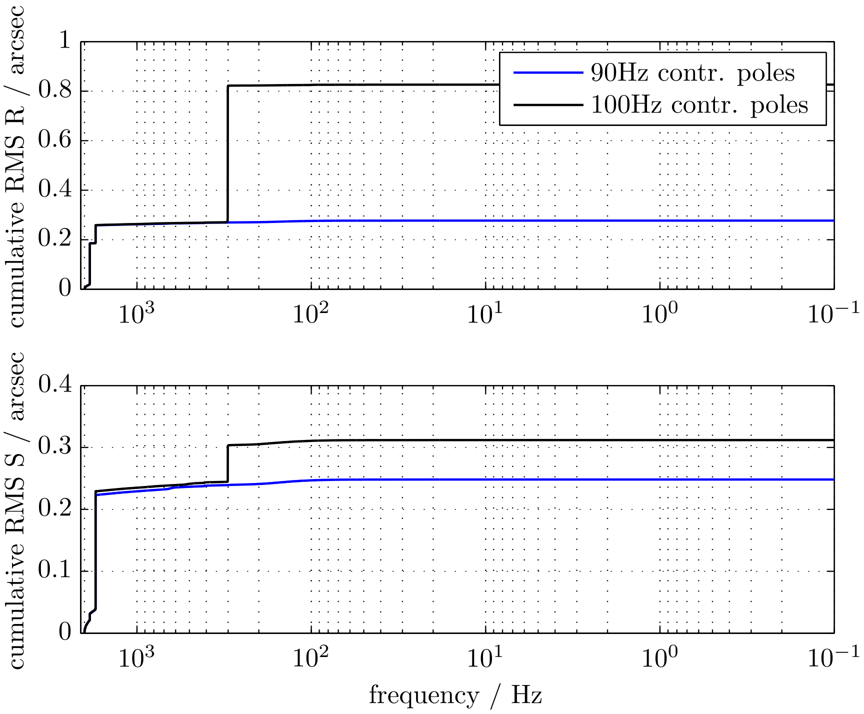

Figure 7: Cumulative RMS in closed loop for different corner frequencies

Controller [Hz]	90	110	120	130	140	150	190
Settle Time [ms]	12.1	10.0	9.6	9.3	8.9	8.8	8.4

Table 3: Settling time for different controller poles

3.1 Observer Adjustment for Bias Correction

According to [8] Kalman Filters are not suitable for estimating biases. Unfortunately, the TCM's iron core actuators exhibit a hysteresis effect that acts as a bias. One approach to handle this deficit would be to include the hysteresis in the observer model. Considering the fact that the hysteresis is amplitude dependent this would add a considerable amount of complexity to the model. Given the limited processing power and the real-time requirement this path was not followed.

A much simpler way is to calculate the output estimation error

$$\tilde{y} = y - \hat{y}, \tag{12}$$

with actual output y and estimated output $\hat{y}$, and add it to the observed position output which is used for the integral part of the controller. All other states are not used for absolute position corrections but only for dynamic corrections, which means in turn, that there is no use in bias correcting them.

Of course, if the estimation error is not filtered or averaged this reintroduces the noise of the position sensors into the closed loop. Therefore the improved steady-state behavior has to be carefully balanced against the potentially increased noise. For a system without delays the described approach would simply replace the estimated position by the measured position. In the case of the TCM with the two step delay however, the output estimation error is the difference between the measured position which arrives with a two time step delay and the two steps delayed estimated position:

$$\tilde{y} = y(k) - \mathbf{H}\hat{\mathbf{x}}(k-2). \tag{13}$$

Correcting the estimated position with equation (13) then results in

$$\hat{y}(k) = \mathbf{H}\hat{\mathbf{x}}(k) - y(k) + \mathbf{H}\hat{\mathbf{x}}(k-2). \tag{14}$$

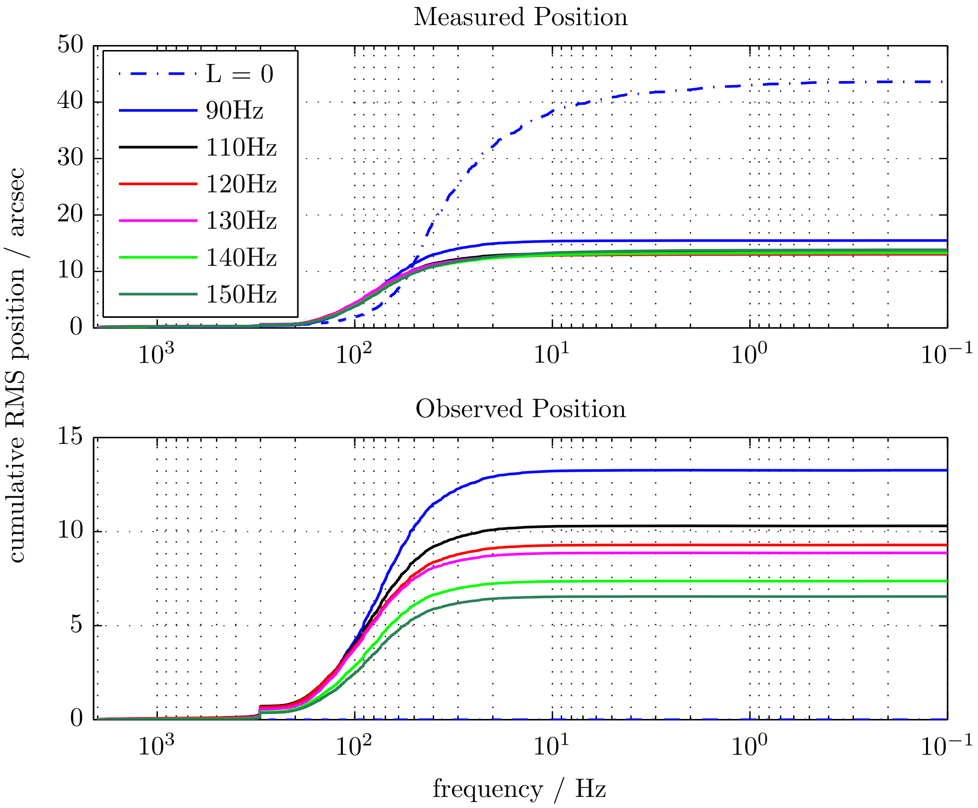

(a) Measured and estimated position

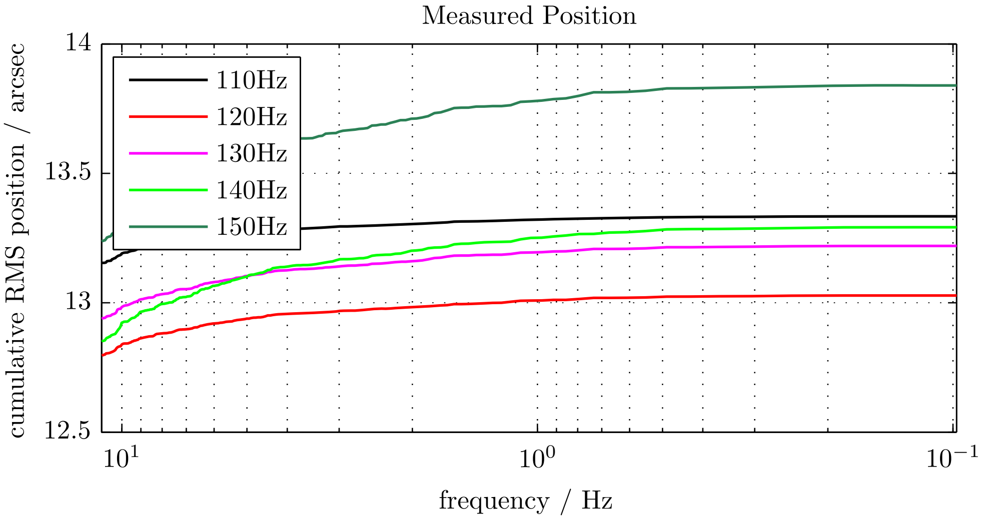

(b) Measured position zoomed in

Figure 8: Cumulative RMS in closed loop for different gain sets

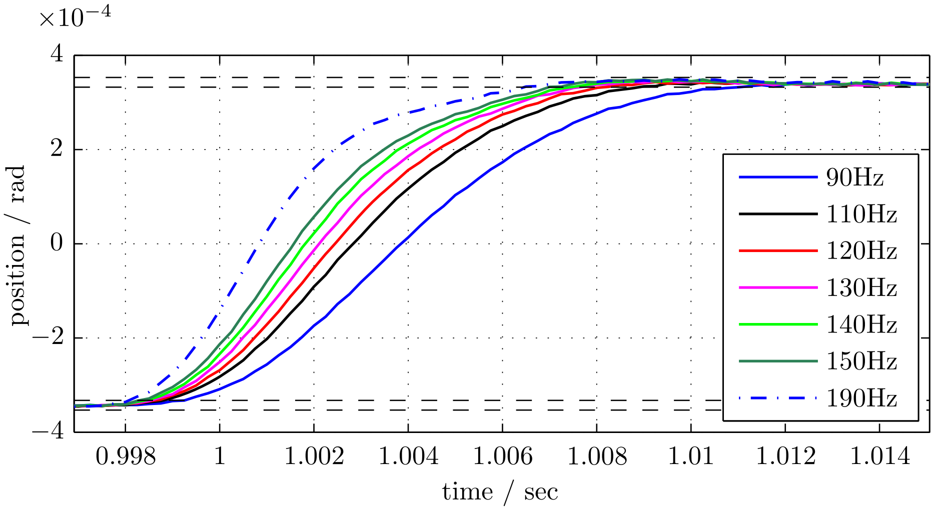

Figure 9: Square Wave for different gain sets

In other words, the current estimated position is corrected by the estimation error of two time steps ago. Since bias corresponds to a static offset rather than any dynamic effect this delayed correction is absolutely sufficient.

Figure 10 shows the measured and estimated position while chopping in open loop mode. The effect of the bias correction can easily be seen the moment it is applied at around time $t = 4.95s$; then the measured and estimated position suddenly are on top of each other.

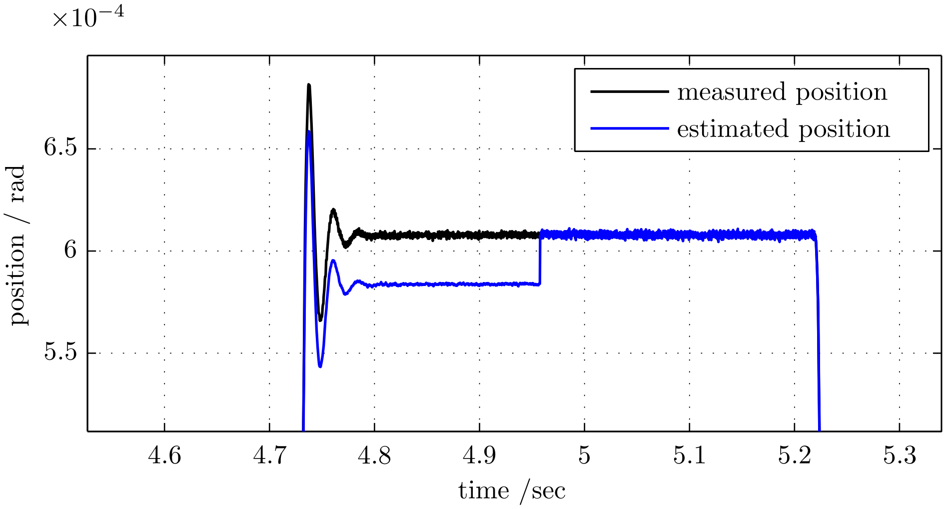

Figure 10: Effect of bias correction on estimated position

Next the effect of the bias correction on the closed loop behavior is examined. Figure 11a shows the mirror position in closed loop mode and the estimated position calculated by a Kalman filter. One can see that there is an offset on the position which is not observed to its full extent by the estimator. Since it is not observed the controller is unaware of it and it is therefore not compensated. At time $t = 4.8s$ the bias correction is activated. This leads to a jump in the observer position, which then matches the actual mirror position, and subsequently to the correction of the undesired deflection.

Figure 11b is produced with the same data and emphasizes the correction of the offset without an increase in noise (no increased diameter of the ”with correction blob”).

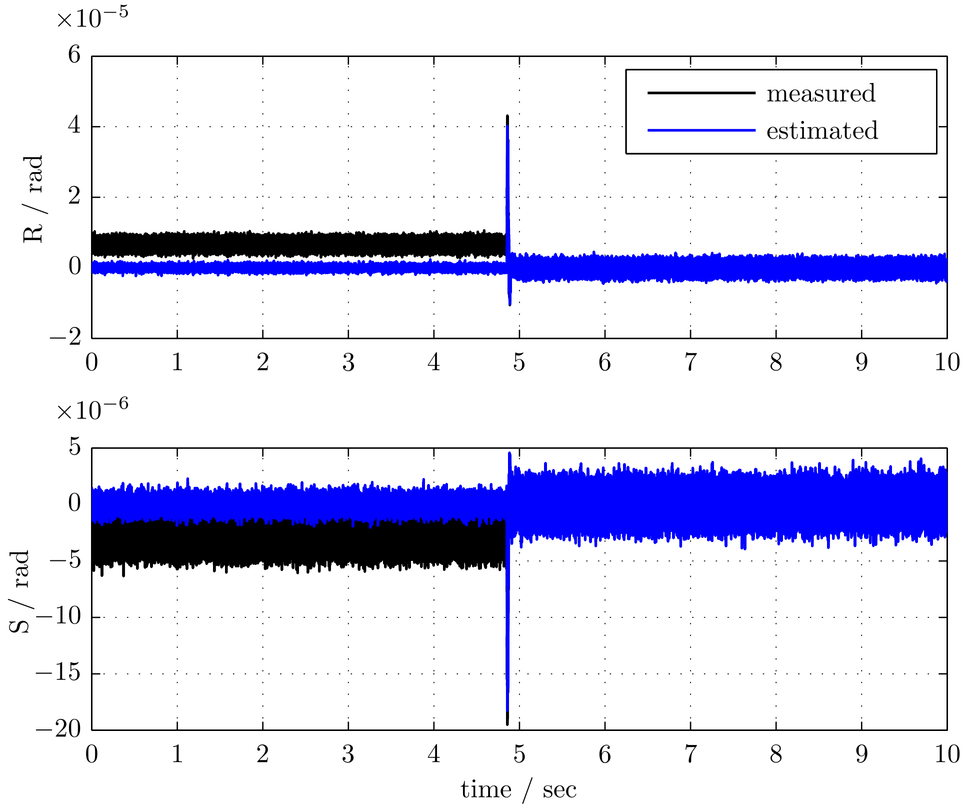

(a) Position vs. time

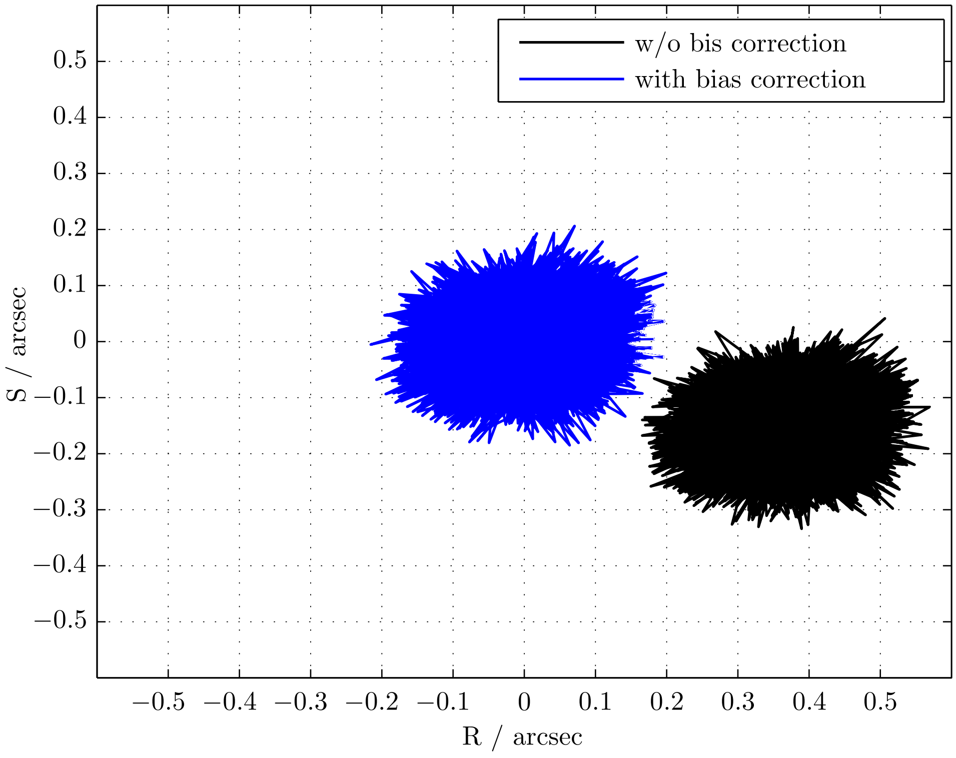

(b) R vs. S

Figure 11: Position with and without bias correction

How the addition of the output estimation error affects the transient of the square wave is shown in figure 12. The left half of the plot is done without bias correction and the right half is chopping with active bias correction.

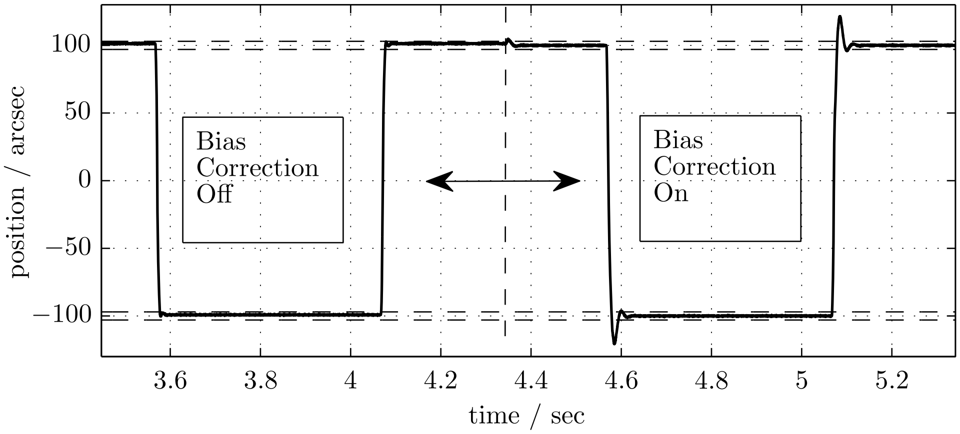

Figure 12: Chopping with corrected and uncorrected position estimate

While the (in this case) small bias gets corrected, the overshoot that is due to the bias correction leads to an intolerable increase in settling time. The overshoot is caused by small errors of the estimated position in the transition phase of the square wave.

Since the correction is not intended to influence the dynamics, but only static offsets low pass filtering of the bias correction is introduced next. Figure 13 shows chopping with bias correction filtered with Butterworth low pass filters with corner frequencies of 1, 10 and 100 Hz compared to unfiltered bias correction. It can be seen,

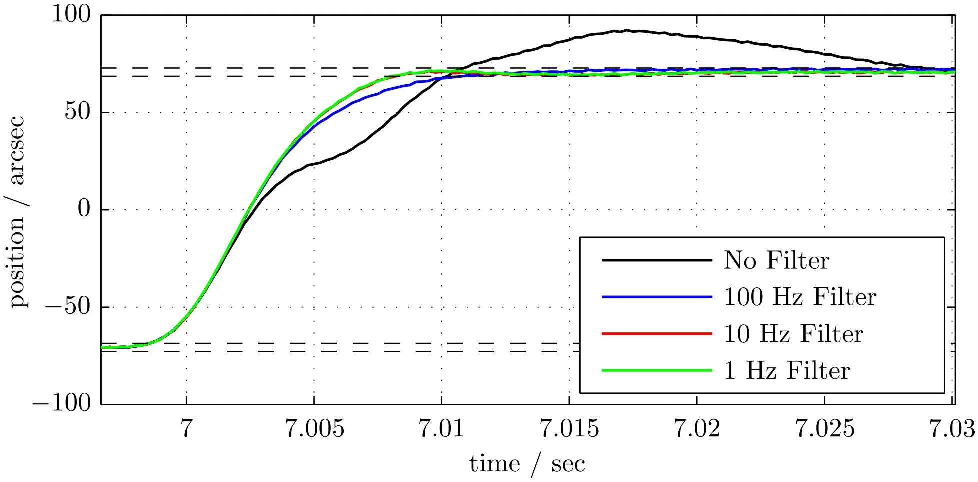

Figure 13: Chopping with filtered correction

that the introduction of the bias correction results in considerable overshoot. This overshoot gets reduced with filtering, While the settling time with the 100 Hz filter is slightly longer, the transients with the 10 and 1 Hz filter are nearly identical. Therefore the 10 Hz filter was chosen for implementation.

4. CURRENT PERFORMANCE DATA

The controller as developed in section 3 has routinely been flying on SOFIA for more than two years now. Its performance in flight is frequently captured and analyzed. Data from flight testing in January 2016 is shown in this chapter.

The TCM tests are divided into two subsets, both of which are comprised by chopping with different amplitudes and chop angles. One subset is focused on the TCM subsystem itself, using as data to be analyzed exclusively the TCM internal position sensors. Consequently, no target star is required. To have cleaner data the Flexible Body Compensation (FBC, which uses the SMA as actuator for pointing corrections, see [9] for more information) is turned off for this subset of tests. Since this approach depends entirely on the accuracy of the position sensors, which are known to have temperature drifts,[3] there is another subset of tests, which relies on centroid data captured by SOFIA's upgraded Focal Plane Imager (FPI+) with the fast readout mode which allows for recording images with frame rates of more than 400 Hz. Obviously a target star is required for these tests and since the FPI+ sees not only TCM moves but all disturbances affecting the telescope FBC is active for these tests.

4.1 Position Sensor Data

Table 4 lists the different settings that were tested with FBC Off.

Test	SMA Status	Chop Amplitude SMARF in arcsec	Chop Throw on sky in arcmin	Chop Angle in deg
1	Standby	0	0.0	0
2	Active	0	0.0	0
3	Active	50	0.4	0
4	Active	100	0.9	0
5	Active	250	2.2	0
6	Active	500	4.5	0
7	Active	750	6.7	0
8	Active	900	8.0	0
9	Active	1125	10.0	0
10	Active	900	8.0	45
11	Active	50	0.4	90
12	Active	100	0.9	90
13	Active	250	2.2	90
14	Active	500	4.5	90
15	Active	750	6.7	90
16	Active	900	8.0	90
17	Active	1125	10.0	90

Table 4: Test Settings with FBC OFF

One run (Test 1) was made with the TCM in Standby, i.e. with a deactivated controller but active amplifiers. Comparing this position sensor data with data from Test 2 with active feedback control allows for evaluating the disturbance rejection capabilities and the effective bandwidth of the controller.

The two graphs on the left in figure 14 are time plots of the two angular positions ROT R and ROT S as calculated from the three position sensor signals. The position offsets and fluctuations in the Standby mode data are primarily resulting from wind loads acting on the Secondary Mirror, and to a lesser degree by aircraft vibrations and wind loads transmitted through the telescope structure.

A reverse cumulative RMS plot of the angular positions in arc seconds on sky is shown on the right hand side of figure 14. As can be seen from the increase at 300 Hz activating the feedback controller slightly excites the

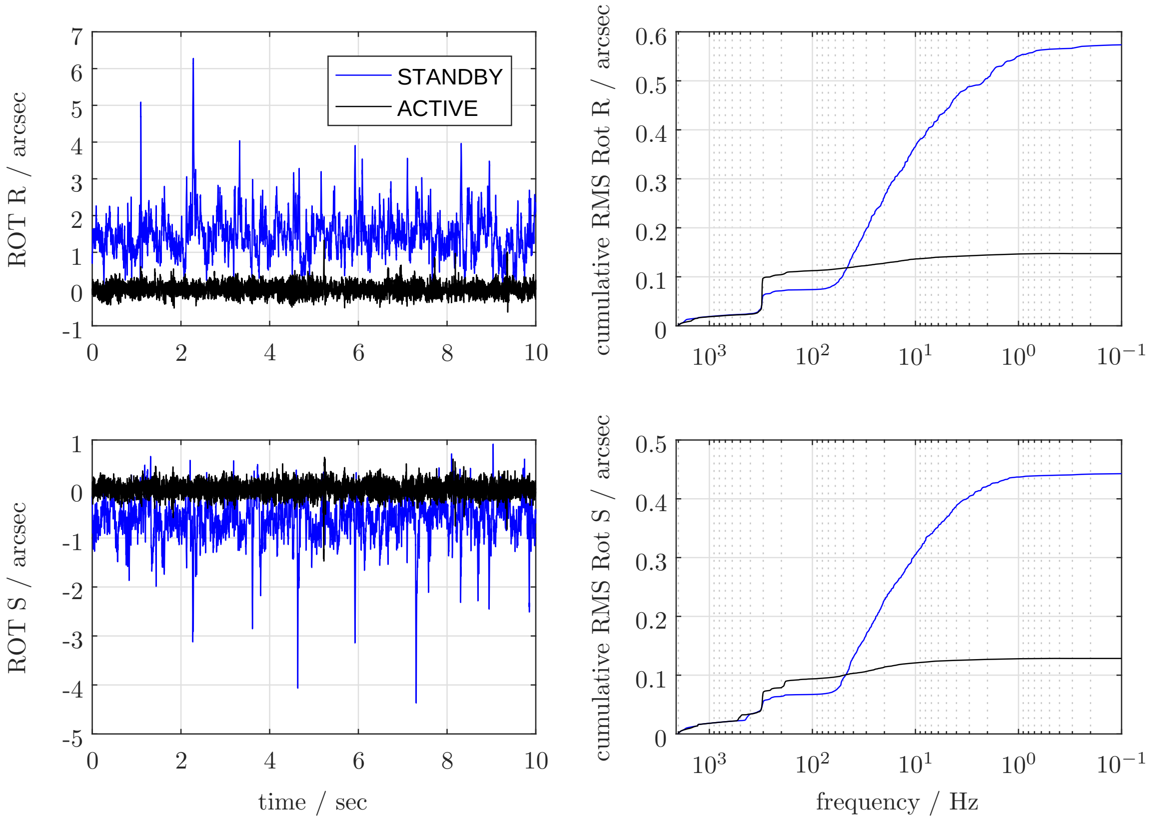

Figure 14: TCM stability with feedback control disabled and enabled

structural mode at this eigenfrequency. Going towards lower frequencies the feedback controller's disturbance rejection begins to take effect at about 70 to 80 Hz. The increase at 300 Hz is then made up for at about 50 Hz.

The total amount of the SM's RMS jitter depends considerably on the environmental conditions, i.e. on the turbulence level. In the present case (in quiet conditions) the RMS of the jitter in ROT R (which results in movements in the elevation direction in the focal plane) gets reduced by the controller from about 0.57 arcsec to 0.15 arcsec, and in ROT S (which results in movements in the cross-elevation direction in the focal plane) from 0.44 arcsec to 0.13 arcsec. Total jitter is thus 0.2 arcsec RMS with the TCM in ACTIVE mode, i.e. with closed feedback control loop.

The other major performance parameter of the TCM, besides the jitter, is the settling time, i.e. the time needed to transition from one chop beam to the next. Figure 15 shows such transitions for all tested amplitudes in the ROT R direction (Test 3 - Test 9). To allow for direct comparison of the various amplitudes the data in this plot was scaled to a medium amplitude of 500 arcsec in the Secondary Mirror Assembly Reference Frame (SMARF). The similarity of the transitions for all amplitudes shows that the closed loop system's linearity is rather good. There are differences however, especially towards very high amplitudes the time to reach 0 (or 50% of the desired amplitude), also called delay time, increases. This is an indication of nonlinearities in the amplifiers performance which are operated close to their performance limits with these high chop amplitudes and short transition times.

The TCM is considered to be settled at its new position once it stays in a 3% region around the desired position. This stability region is indicated with the dashed lines in figure 15. The controller is designed so that the rise time equals the settling time, or in other words the overshoot does not exceed the stability region. The settling time (transition between stability regions) is between 10 and 11 milliseconds for all tested amplitudes and chop angles.

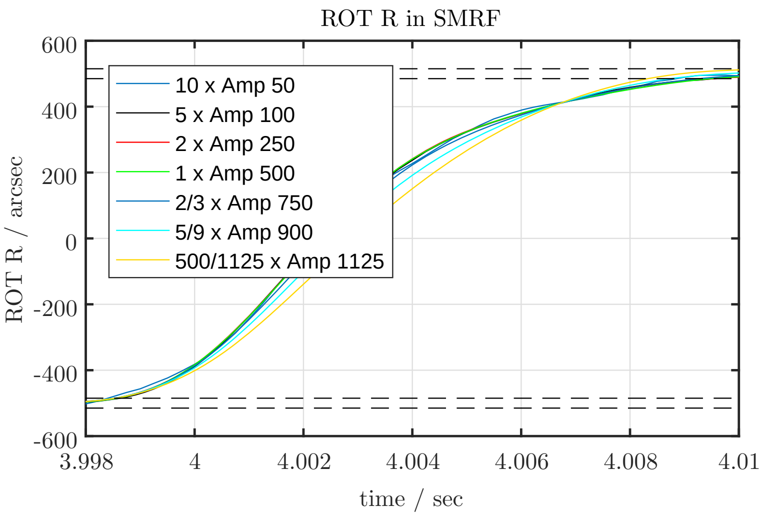

Figure 15: Settling Time for all amplitudes with chop angle 0°

4.2 FPI+ Data

Table 5 lists the different settings that were tested with FBC On.

Test	SMA Status	Chop Amplitude SMARF in arcsec	Chop Throw on sky in arcmin	Chop Angle in deg
18	Standby	0	0.0	0
19	Active	0	0.0	0
27	Active	50	0.4	0
28	Active	100	0.9	0
29	Active	250	2.2	0
30	Active	500	4.5	0
31	Active	750	6.7	0
32	Active	900	8.0	0

Table 5: Test Settings with FBC ON

For TCM performance analysis looking at FPI+ data is mainly needed to verify angle and amplitude precision because the TCM internal position sensors which are used for the closed loop control are known to vary with temperature. The Tilt Scale which translates deflection amplitudes from the SMARF to sky values was set to 3.7387. Postflight, this factor was then also used for translating the position sensor data into sky values for comparison with the FPI+ centroid data.

The TCM's stability with and without feedback control (Test 19 and Test 18) is shown in a reverse cumulative RMS plot for both axes combined in figure 16 in arc seconds on the sky. The FPI+ was sampled with 411 Hz while the internal TCM position sensors are sampled with 4 kHz. For sake of better comparison, the sensor data was resampled with 411 Hz and is plotted in dashed lines.

Comparing the RMS of the original sensor data with the resampled data shows a significant difference in the Active case (Test 19). The reason for that becomes clear when looking at the Power Spectral Density (PSD) plot in figure 17. In Test 19 there is significant excitation in ROT R of a TCM eigenmode at about 300 Hz (in this case it is at 306.9 Hz) which is beyond the FPI+'s Nyquist frequency (205.6 Hz) for this test run. The appearance of the 300 Hz mode in the FPI+ data can be modeled by averaging the 4 kHz TCM position sensor data over each FPI sampling interval, thereby resampling the position sensor data.

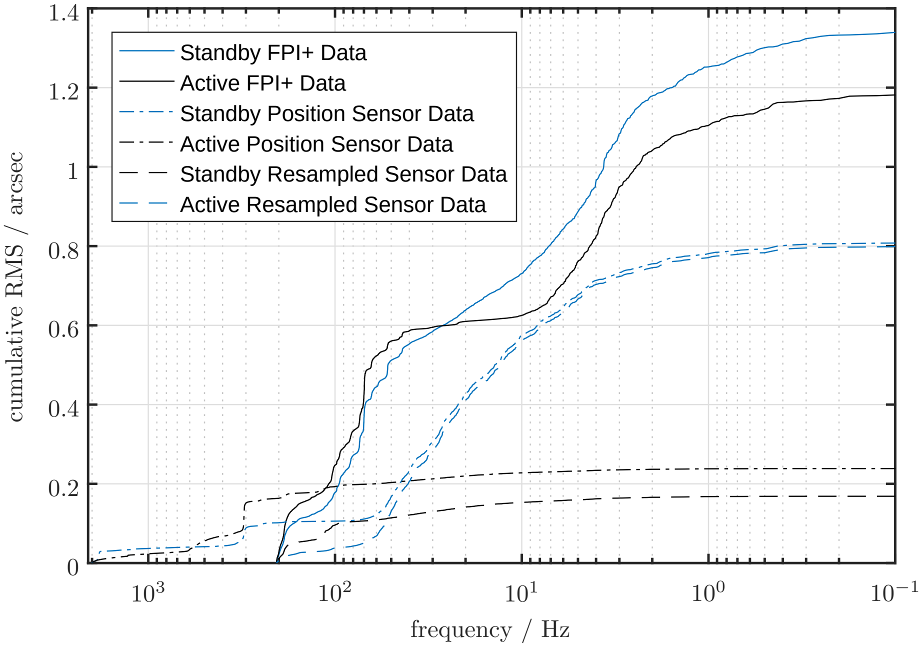

Figure 16: TCM stability in Standby and Active Mode

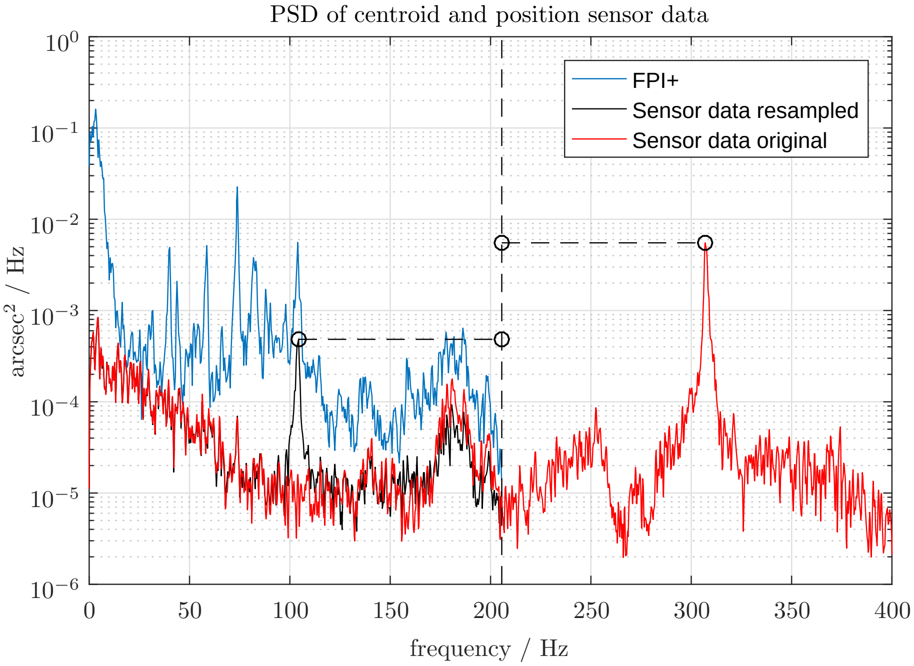

Figure 17: Power Spectral Density of Test 19 ROT R

Then about 10% of the energy contained in the 300 Hz peak show up in the resampled data and in the FPI+ data at 104.4 Hz, which is the actual vibration frequency mirrored at the Nyquist frequency. The remainder of the vibration cannot be resolved and instead translates into an increase of image size rather than centroid motion.

The power spectral density plot of the FPI+ data with deactivated and activated TCM in figure 18 confirms that the frequency peak at 104.4 Hz is indeed caused by the 300 Hz mode of the active TCM. The peak does not exist in Standby mode with deactivated controller.

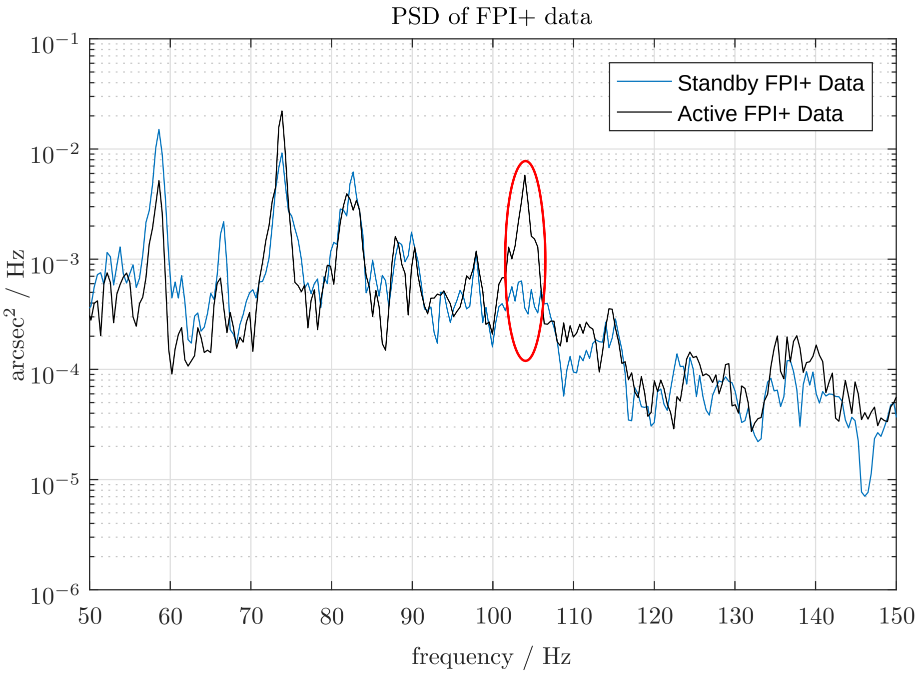

Figure 18: Power Spectral Density of Test 18 and 19

Figure 19 compares position sensor data with centroid data as measured in the focal plane for the smallest tested chop amplitude (Test 27, 50 arcsec) and the largest tested chop amplitude(Test 32, 900 arcsec). Tests 28 – 31 with amplitudes between those extremes look very similar and are therefore not shown here. Generally, the agreement between the two data sets is excellent, confirming the good temperature calibration of the position

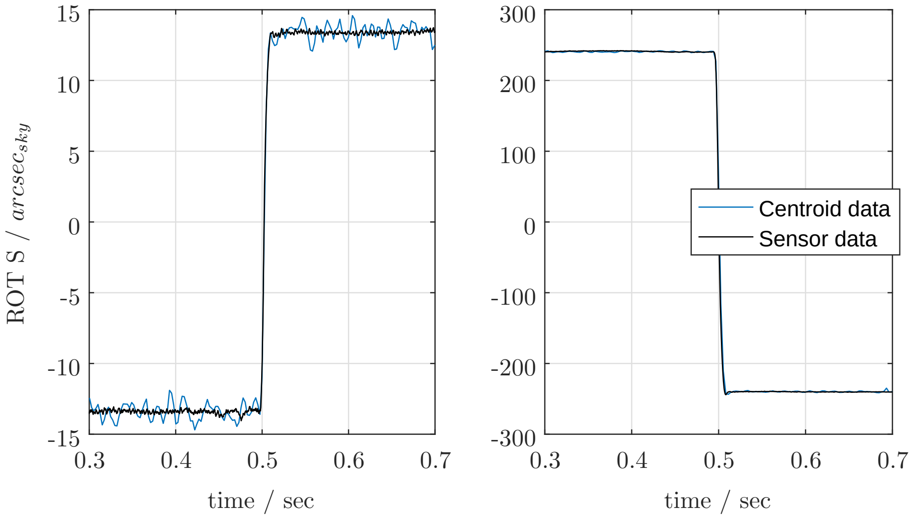

Figure 19: Centroid and sensor data for small (left) and large (right) chop throw

sensors (for details about the temperature calibration of the sensors see [3]). The data was taken at TCM actuator temperatures of around $-29°C$.

In the centroid data in the left-hand plot the pointing jitter is clearly visible. This is caused by unintended telescope motions, not by the TCM. For this run FBC was still off, therefore the pointing jitter is relatively high and the TCM motion relatively small.

The TCM's main performance figures are listed in table 6.

Bandwidth (90 Hz Phase Delay)	50 Hz
Settling Time for all amplitudes	10 - 11 ms
Stability on sky (quiet conditions)	<0.3 arcsec RMS

Table 6: TCM performance parameters

5. SUMMARY

The state space model of SOFIA's Tilt Chop Mechanism is based on the equations of motion of the system and on the electrical motor equations. The model parameters were then adjusted to achieve a good fit with input/output data measured with the TCM installed on the telescope. Some crucial features not covered in the linear model were then added, namely the actuator hysteresis, a feedback delay, a dominant flexible mode, a temperature dependency, and an amplitude dependent nonlinearity. This model was then discretized, implemented in the real-time control software, and supplied with a Kalman gain to estimate the required states actuator current, angular position and angular velocity.

Using pole placement, controller gains were identified that guarantee optimal square wave behavior to achieve good chopping performance. The Kalman gain was determined in combination with the controller gains to achieve the best possible trade-off between closed loop system bandwidth and sensor noise influx. The main factor preventing a higher closed loop bandwidth is the desire to limit the excitation of the eigenmode at 300 Hz while still maintaining a reasonably good disturbance rejection. This mode is described in detail in 10 and there are investigations underway to add structural damping to this mode to enable a faster controller.

To compensate for the unsatisfactory bias estimation of the Kalman filter an additional term was introduced that adds the lowpass filtered difference between estimated and measured angular position. Then data is presented that was gathered on a SOFIA flight in the beginning of 2016. It is shown how the remaining vibrations at 300 Hz are reflected in the focal plane camera data recorded with 400 Hz and the main performance parameters settling time, stability, and bandwidth are presented.

REFERENCES

[1] L. Zago, P. M. Genequand, and J. Moerschell, "Extremely compact secondary mirror unit for the sofia telescope capable of 6-degree-of-freedom alignment plus chopping," in *Advanced Technology Optical IR Telescopes VI*, L. M. Stepp, ed., *Proc. SPIE* **3352**, pp. 666–674, 1998.

[2] A. Reinacher, *Inflight Commissioning and Performance Improvement of the SOFIA Secondary Mirror Mechanism*. PhD thesis, University of Stuttgart, 2014.

[3] Y. Lammen, A. Reinacher, I. Kjelberg, S. Droz, H. Jakob, F. Graf, and A. Krabbe, "Sofia secondary mirror mechanism heavy maintenace and improvements," in *not yet published*, *Proc. SPIE*, 2016.

[4] A. Reinacher and H.-P. Röser, "Modeling of the sofia secondary mirror controller," in *Integrated Modeling of Complex Optomechanical Systems*, **8336**, International Society for Optics and Photonics, 2011.

[5] G. F. Franklin, J. D. Powell, and A. Emami-Naeini, *Feedback Control of Dynamic Systems*, Pearson, 6 ed., 2010. International Edition.

[6] A. Reinacher, E. Onillon, and H.-P. Röser, “Improvement of the sofia secondary mirror controller,” in *SPIE Astronomical Telescopes and Instrumentation: Observational Frontiers of Astronomy for the New Decade*, **7733**, International Society for Optics and Photonics, 2010.

[7] G. F. Franklin, J. D. Powell, and M. Workman, *Digital Control of Dynamic Systems*, Ellis-Kagle Press, Half Moon Bay, CA, 3 ed., 1997.

[8] P. Zarchan and H. Musoff, *Fundamentals of Kalman Filtering: A Practical Approach*, vol. 208 of *Progress in Astronautics and Aeronautics*, AIAA, 2 ed., 2010. International Edition.

[9] F. Graf, A. Reinacher, H. Jakob, U. Lampater, E. Pfueller, M. Wiedemann, J. Wolf, and S. Fasoulas, “Pointing and control system performance and improvement strategies for the sofia airborne telescope,” in *not yet published*, *Proc. SPIE*, 2016.

[10] B. Greiner, Y. Lammen, A. Reinacher, A. Krabbe, and J. Wagner, “Characterization of the mechanical properties of the sofia secondary mirror mechanism in a multi-stage approach,” in *not yet published*, *Proc. SPIE*, 2016.

SOFIA, the "Stratospheric Observatory for Infrared Astronomy" is a joint project of the Deutsches Zentrum für Luft- und Raumfahrt e.V. (DLR; German Aerospace Centre, grant: 50OK0901) and the National Aeronautics and Space Administration (NASA). It is funded on behalf of DLR by the Federal Ministry of Economics and Technology based on legislation by the German Parliament, the state of Baden-Württemberg and the Universität Stuttgart. Scientific operation for Germany is coordinated by the German SOFIA-Institute (DSI) of the Universität Stuttgart, in the USA by the Universities Space Research Association (USRA).